Liu, S., Zhang, Y., Li, M., Xiong, L., Zhang, Z., Yang, X., He, X., Wang, K., Liu, J., & Mann, S. (2020). Enzyme-mediated nitric oxide production in vasoactive erythrocyte membrane-enclosed coacervate protocells. *Nature Chemistry*, *12*, 1165–1173. https://doi.org/10.1038/s41557-020-00585-y

Enzyme-mediated nitric oxide production in vasoactive erythrocyte membrane-enclosed coacervate protocells

Songyang Liu,[1] Yanwen Zhang,[1] Mei Li,[2] Li Xiong,[3] Zijian Zhang,[3] Xiaohai Yang,[1] Xiaoxiao He,[1] Kemin Wang,[1] Jianbo Liu,[1,2*] Stephen Mann[2*]

[1] State Key Laboratory of Chemo/Biosensing and Chemometrics, College of Chemistry and Chemical Engineering, Key Laboratory for Bio-Nanotechnology and Molecular Engineering of Hunan Province, Hunan University, Changsha 410082, P. R. China. Email: liujianbo@hnu.edu.cn.
[2] Centre for Protolife Research, School of Chemistry, University of Bristol, Bristol. BS8 1TS, UK. Email: s.mann@bristol.ac.uk.
[3] The Second Xiangya Hospital, Central South University, Changsha 410008, P. R. China.

The design and construction of synthetic therapeutic protocells capable of establishing cognate chemical communication channels with living cells is an important challenge for synthetic biology and bio-engineering. Here we develop a step towards protocell-mediated nitric oxide-induced vasodilation by constructing a novel synthetic cell model based on bio-derived coacervate vesicles with high hemocompatibility and increased blood circulation times. The hybrid protocells are prepared by the spontaneous self-assembly of hemoglobin (Hb)-containing erythrocyte membrane fragments on the surface of preformed polysaccharide/polynucleotide coacervate micro-droplets containing glucose oxidase (GOx). We use the sequestered enzymes to program a spatially coupled GOx/Hb reaction cascade, which in the presence of glucose and hydroxyurea generates a protocell-mediated flux of nitric oxide that we exploit for *in vitro* and *in vivo* blood vessel vasodilation. Taken together, our results provide new opportunities for the development of endogenously organized cell-like entities (biocompatible micro-bots) geared specifically towards active interfacing with individual living cells and cell communities.

The development of biocompatible artificial constructs capable of microscale chemical communication and bilateral signalling at the living/non-living interface is an important challenge for synthetic biology and bio-engineering[1,2]. Synthetic cell-like micro-compartments in the form of phospholipid vesicles (liposomes) have had a major impact as non-viral vectors for targeted drug delivery [3], tissue engineering [4], gene therapy [5] and imaging [6]. These applications exploit liposomes as smart but essentially chemically passive synthetic micro-compartments, rather than as interactive micro-reactors capable of establishing cognate communication channels with living cells. In this regard, recent advances in the design and construction of non-lipid synthetic protocells have produced a platform of alternative technologies for preparing endogenously organized microscale objects with increased robustness, membrane programmability and life-like agency. In particular, augmented semi-permeable membrane structures have been engineered in polymersomes [7,8], colloidosomes [9] and proteinosomes [10,11], giving rise to collective protocell behaviours such as motility [12,13], phagocytosis [14], predation [15], DNA-based computation [16], chemical communication [17-20] and reversible contractibility [21]. Alternatively, biochemical and biomimetic functions have been internalized within membrane-free molecularly crowded coacervate micro-droplets [22] and soft hydrogel microparticles [23] to generate coordinated behaviours such as artificial endocytosis and parasitism [24], signalling [25] and RNA catalysis [26,27]. Given these recent advances, it seems timely to explore the use of cell-like entities as biocompatible micro-bots geared specifically towards active interfacing with individual living cells and cell communities.

Although polymersome-based nanoreactors typically 100 nm in size have been used widely as artificial organelles for the *in vitro* [28-32] and *in vivo* [33] uptake and activation of intracellular reactions, there are few examples of micrometer-scale architectures being developed as chemically active synthetic therapeutic cells. In principle, these programmable constructs represent archetypes of autonomic soft micro-machines capable of sensing cellular environments and providing cognate responses via chemical activation and feedback. To date, protocell signaling has been coupled to bacterial communities [34-36], antigen-labelled colloidosomes (Pickering emulsions) used to enhance the uptake, recruitment and activation of antigen-presenting mouse cells [37], hydrogel-containing proteinosomes exploited for the

intracellular killing of cancer cells [38], and multi-compartmentalized lipid vesicles comprising a glucose-metabolism system and membrane-fusion machinery used as synthetic beta cells for fusion-mediated dynamic insulin secretion [39].

In this paper we use cell-sized coacervate micro-droplets derived from electrostatically mediated liquid-liquid phase separation as the basis for a new approach to the potential development of synthetic therapeutic protocells capable of generating a nitric oxide signal for *in vitro* and *in vivo* blood vessel vasodilation. Coacervate droplets exhibit high levels of biomolecule sequestration, promote enzyme activities and support cell-free gene expression[22,40-42], are stabilized by ultra-thin coatings of fatty acids [43], block copolymers [44] or silica nanoparticles [45], and can be encapsulated within liposomes [46,47] and proteinosomes [48]. Although many reports have addressed the construction and biomimetic behaviours of coacervate protocells, there are relatively few investigations concerning the use of coacervates for developing biomedical applications [49-52]. Here we develop a first step towards a membrane-enclosed therapeutic protocell based on the spontaneous self-assembly of hemoglobin (Hb)-containing erythrocyte membrane fragments on the surface of preformed polysaccharide/polynucleotide coacervate micro-droplets containing glucose oxidase (GOx) (Fig. 1a). Encapsulation within a thin envelope of erythrocyte membrane fragments provides a physical barrier that minimises contact between the coacervate vesicles and natural erythrocytes, which in turn significantly improves hemocompatibility [53-55] and extends the blood circulation time. We utilise the sequestered enzymes to program a spatially coupled reaction cascade that in the presence of glucose and hydroxyurea generates a protocell-induced flux of nitric oxide (NO) *in vitro* and *in vivo* (Fig. 1b). Based on the endogenous NO production, we demonstrate the onset of protocell-mediated blood vessel vasodilation in a model system of pre-contracted thoracic artery rings. Finally, as a proof-of-concept, we exploit the high hemocompatibility and improved blood circulation of the NO-producing coacervate vesicles to demonstrate the possibility of *in vivo* vasodilation within a perfused rabbit carotid artery.

Results and discussion

Construction of erythrocyte membrane- enclosed coacervate vesicles. Aqueous suspensions of membrane-enclosed polysaccharide-polynucleotide protocells were produced at pH 7 by the spontaneous interfacial assembly of negatively charged erythrocyte membrane fragments on the surface of preformed positively charged coacervate micro-droplets prepared by mixing diethylaminoethyl-dextran chloride (DEAE-dextran, M_w = 500 kDa, 10 mg·mL^{-1}) and double-stranded deoxyribonucleic acid (*ds*DNA, low molecular weight fraction, salmon sperm, 10 mg·mL^{-1}) at a DEAE-dextran : DNA weight ratio of 2 : 1. Prior to addition of the membrane fragments, optical and fluorescence microscopy images showed a polydisperse population of membrane-free spherical coacervate droplets with diameters up to 20 µm (Figs 2a,b). Glucose oxidase (GOx, 0.02 mg mL^{-1}; often labelled with fluorescein isothiocyanate (FITC), partition constant, 85; encapsulation efficiency, 85%; Supplementary Fig. 1a) was sequestered homogeneously into the molecularly crowded coacervate interior during micro-droplet formation (Supplementary Fig. 2). To prepare biomembrane-bounded coacervate droplets, an aqueous suspension of sub-micrometre-sized erythrocyte membrane fragments was prepared by hypotonic hemolysis (Supplementary Fig. 3) and added to a dispersion of the DEAE-dextran/*ds*DNA coacervate droplets (10 mg mL^{-1}; fragments : droplets = 1 : 20, w/w). This resulted in a size increase from 5.4 ± 1.9 to 6.3 ± 1.6 µm (Supplementary Fig. 4) and reversal of the zeta potential from +15.1 ± 1.7 to -10.5 ± 2.9 mV; the latter being close to the surface potential determined for the extracted membrane fragments alone (Fig. 2c and Supplementary Fig. 5). Formation of a continuous erythrocyte membrane-derived shell on the surface of the coacervate droplets was confirmed by optical and fluorescence microscopy images after treating the hybrid protocells with a lipid stain (Figs 2d,e). Corresponding images and fluorescence line profiles of single protocells stained for DNA and lipid confirmed the presence of a homogeneous coacervate interior enclosed within an intact shell of erythrocyte membrane fragments (Figs 2f,g). Electrostatically induced accumulation of the lipid fragments gave rise to an irregular surface texture with variations in the membrane thickness ranging from 0.2 to 1.0 µm in the 3D reconstructed fluorescence microscopy images of individual droplets (Fig. 2h).

FTIR spectra showed characteristic protein and phospholipid absorbance bands for samples of the membrane fragments and membrane-enclosed coacervate vesicles but not for the membrane-free coacervates (Supplementary Fig. 6). Typically, the lipid and protein mass fractions were 42.5 and 45.8% by dry weight (Supplementary Figs. 7 and 8). Gel electrophoresis of the extracted membrane fragments indicated that haemoglobin (Hb; subunit band at 14.4 kDa) was present in the lysate (Supplementary Fig. 9), typically at concentrations of approximately 0.1 mg mL^{-1} (Supplementary Fig. 10). Significantly, considerable levels of Hb were also observed in samples of the coated coacervate droplets (Supplementary Fig. 9), indicating that formation of the membrane-derived shell occurred simultaneously with the transfer of erythrocyte proteins. In this regard, fluorescence microscopy images revealed that the transferred Hb was located specifically on the surface of the coacervate droplets along with the lipid membrane fragments (Fig. 2i).

Hemocompatibility of coacervate-based protocells. Incubation of DEAE-dextran/*ds*DNA coacervate micro-droplets in an isotonic suspension of erythrocytes indicated that the membrane-free protocells exhibited considerably higher *in vitro* hemolytic activity compared with the erythrocyte membrane-enclosed coacervate vesicles (Fig. 3a). Levels of hemolysis increased rapidly as the concentration of uncoated droplets was increased such that values of over 90% were attained after 90 min at coacervate concentrations above 2.25 mg·mL^{-1} (Fig. 3b). In contrast, less than 20% hemolytic activity was observed for erythrocytes incubated with coated droplets under the same isotonic conditions (Figs 3b,c). For example, only 2.6% hemolysis was observed after 90 min at an enclosed protocell concentration of 0.6 mg mL^{-1}. We attributed the increase in hemocompatibility to the blocking of deleterious contact interactions between the negatively charged red blood cells (Fig. S5) and positively charged coacervate matrix (Fig. 2c) in the presence of the negatively charged shell of erythrocyte fragments (Fig. 2c). This was consistent with fluorescence confocal microscopy images, which showed minimal levels of surface contact between the coacervate vesicles and erythrocytes (Supplementary Fig. 11).

Given the above observations, we used fluorescence-activated cell sorting (FACS) to monitor changes in the population dynamics in binary communities of erythrocytes and

coacervate-based protocells prepared in isotonic solutions at an initial droplet : erythrocyte number ratio of 1 : 4. 2D dot plots of forward light scattered-height (FSC-H) versus side light scattered-height (SSC-H) indicated that single populations of native coacervate droplets, erythrocyte membrane-enclosed coacervate droplets and erythrocytes showed distinct scattering profiles (Figs 3d,e and i,j). As a consequence, we tracked the changes in the numbers of protocells and living cells present in freshly mixed binary populations over a period of 90 min (Figs 3f-h and k-m). While a progressive depletion of the red blood cell population was observed in mixtures of native coacervate droplets and erythrocytes, minimal changes in the population number densities were determined for binary communities of the red blood cells and biomembrane-enclosed coacervate vesicles. In the former case, a new sub-population of erythrocyte membrane-enclosed coacervate droplets with relatively low FSC-H and high SSC-H values was observed (Fig. 3h), suggesting that hemolysis resulted in the coacervate droplets becoming coated *in situ* in released membrane fragments. Time-dependent FACS analysis indicated that addition of the membrane-free coacervate droplets resulted in a rapid decrease in the number of red blood cells to *ca.* 55% over an initial period of 5 min, after which the rate of hemolysis decreased until only 6 % of the erythrocyte population remained after 90 min (Figs 3n,o). In comparison, the percentages of erythrocytes present after 5 and 90 min were 98 and 92 %, respectively, in mixtures containing the biomembrane fragment-enclosed droplets (Figs 3p,q). No significant changes in the FACS scattering plots were observed in control experiments involving single populations of erythrocytes, coacervate droplets, or membrane-enclosed coacervate droplets (Supplementary Fig. 12). The latter were also stable in serum for at least 90 min; in contrast, the membrane-free coacervate droplets coalesced into a bulk phase within 60 min (Supplementary Fig. 13).

Blood circulation and tissue biodistribution. Given that membrane encapsulation of the DEAE-dextran/*ds*DNA coacervate droplets considerably improved their hemocompatibility, we reasoned that this would also extend their blood circulation times. *In vivo* experiments were conducted using erythrocyte-membrane enclosed coacervate vesicles containing sequestered sulfo-cyanine 5 carboxylic acid (Cy5) as a fluorescent marker. A suspension of the Cy5-loaded

protocells was intravenously injected into a group of six rabbits and samples of blood collected at various time points. The blood clearance profiles indicated that approximately 25% of the injected population of coacervate vesicles was retained in the blood after 2 h (Fig. 4a). In contrast, the uncoated coacervate droplets were rapidly cleared from the blood stream with a retention of only 8 % after 2 h (Fig. 4a). Based on the pharmacokinetic profiles, the elimination half-lifes were 31.0 and 16.1 min for the membrane-enclosed and uncoated coacervate droplets, respectively.

Fluorescence imaging was used to investigate the biodistribution of the Cy5-loaded coacervate vesicles in a range of major tissues analysed 2 and 24 h after injection (Fig. 4b). High fluorescence intensities were observed after 2 h specifically in the liver, spleen and kidney, as well as in blood. In each tissue, the fluorescence markedly decreased after 24 h. Quantitative analysis confirmed that the accumulated protocell content per gram of tissue after 2 and 24 h was highest in the liver and spleen, followed by lower but significant levels in the kidney, lung and blood at 2 but not 24 h (Fig. 4c). When normalized to the total fluorescence, the relative signal intensities after 2 h were dominant for the liver and blood (Fig. 4d). In contrast, only the liver showed a normalized fluorescence output after 24 h (Fig. 4d), indicative of accumulation and degradation of the coacervate vesicles via metabolic pathways of the liver.

Protocell-mediated generation of NO. As the Hb present in the erythrocyte membrane extract exhibited high peroxidase-like activity (Fig. 5a), we sought to exploit the bio-enclosed coacervate vesicles as a new type of synthetic protocell capable of generating nitric oxide (NO) in the presence of hydroxyurea and H_2O_2 [56]. To achieve this, we spatially coupled Hb-mediated production of NO at the erythrocyte shell surface with the endogenous generation of a localized H_2O_2 signal by sequestering GOx within the DEAE-dextran/*ds*DNA matrix and using glucose (5 mM) as the input to initiate the cascade reaction in the presence of hydroxyurea (2 mM) (Fig. 5b). Under these conditions, the coacervate vesicles produced NO typically with initial rates of *ca.* 0.25 μM·min^{-1} and yields of up to 8.7 μM over a reaction period of 180 min. The production of NO was dependent on the glucose and hydroxyurea concentrations for a constant protocell number density (Supplementary Fig. 14). In contrast, negligible NO was produced in the absence

of GOx or without the erythrocyte membrane fragments (Fig. 5b), or when the coacervate micro-droplets were coated in the zwitterionic phospholipid dipalmitoylphosphatidylcholine (Supplementary Fig. 15). The spatial localization of H_2O_2 (GOx activity) and NO (Hb activity) production within the protocells was confirmed from fluorescence microscopy images of single biomembrane-enclosed coacervate vesicles prepared in the presence of Amplex Red and DAF-2 (2-(3,6-dihydroxy-4,5-diamino-9H-xanthen-9-yl)-benzoic acid). On addition of glucose, peroxidation of Amplex Red gave rise to a rapid increase in red fluorescence specifically within the coacervate interior due to formation and retention of resorufin (Figs 5c,d). At the same time, reaction of DAF-2 with nitrite produced by NO oxidation in water resulted in a progressive increase in green fluorescence initially within the protocell (Figs 5e,f). As the Hb was located predominantly at the membrane surface, we attributed the increase in green fluorescence within the coacervate phase to the selective partitioning of DAF-2 (K=140, Supplementary Fig. 1b) and diffusion of NO into the protocell interior. With time, green fluorescence was also observed outside the protocells (Fig. 5e), indicating that NO and nitrite were slowly released into the external environment as the cascade reaction proceeded.

***In vitro* NO generation and blood vessel vasodilation.** Given the NO-generating capacity of the erythrocyte membrane- enclosed GOx-containing coacervate vesicles, we investigated their potential as synthetic protocells capable of triggering the NO-mediated biochemical pathway for blood vessel vasodilation *in vitro.* The hybrid protocells were incubated in the presence of glucose with a 5 mm-wide section of a pre-contracted thoracic aorta connected to a force transducer (Supplementary Figs. 16, 17)[57,58]. Protocell-mediated production of NO was initiated immediately by addition of hydroxyurea, which gave rise to a concomitant decrease in the recorded isometric tension force associated with the aortic ring (Fig. 6a). In contrast, minimal changes were observed when GOx-free hybrid protocells were used in the experiments (Fig. 6b). Typically, the enzymatically active protocells produced NO levels of up to 1.3 μM, which gave rise to a tension force decrease of 5.0 g and a blood vessel relaxation of 38% (Fig. 6c). Moreover, sequential addition of aliquots of hydroxyurea produced a stepwise decrease in the tension force

(Supplementary Fig. 18), confirming that the protocell-mediated generation of NO within the aortic rings was sufficient to induce vasodilation in the pre-contracted tissue.

***In vivo* NO generation in blood vessel tissue.** Based on the above results and given the hemocompatibility and improved blood circulation profile of the erythrocyte membrane-enclosed coacervate vesicles, we investigated whether the GOx-containing protocells could be used for the *in vivo* generation of NO in blood vessel tissue. To address this challenge, a safe dose of GOx-loaded coacervate vesicles together with hydroxyurea was intravenously injected into a rabbit carotid artery (Supplementary Fig. 19). We reasoned that the endogenous concentration of blood glucose would be sufficient to trigger the protocell-induced spatially coupled GOx/Hb cascade reaction, thereby increasing the levels of NO in the blood stream and surrounding blood vessels. Time-dependent monitoring over a period of 20 min after injection showed a progressive increase in the concentration of blood NO, reaching a value of 210 ± 60 nM after 10 minutes (Fig. 6d). The raised NO levels were considerably lower than the threshold value for NO-mediated cell toxicity[59]. The *in vivo* generation of NO was also confirmed by fluorescence imaging of the extracted blood vessels after staining with the NO intracellular probe, diaminofluorescein-FM diacetate (DAF-FM DA, green fluorescence). High levels of green fluorescence were observed in sections of the blood vessel tissue after injection of the GOx-containing erythrocyte membrane-enclosed coacervate vesicles (Fig. 6e-g). In comparison, minimal levels of green fluorescence were observed in blood vessel sections when GOx-free coacervate vesicles or hydroxyurea alone were injected into the animals (Supplementary Fig. 20), confirming that the protocell-confined GOx/Hb enzyme cascade was sufficiently active *in vivo* to increase the NO concentration within the blood vessels.

***In vivo* blood vessel vasodilation.** Given that we were able to detect levels of NO in blood vessel tissue (210 ± 60 nM) well above those generally considered to stimulate vasodilation (10 nM)[60] and the ability of the GOx-containing erythrocyte membrane-enclosed coacervate vesicles to induce *in vitro* vasodilation in pre-contracted thoracic aorta, we explored as a proof-of-principle whether the protocells were capable of triggering the NO-mediated biochemical pathway for

blood vessel vasodilation *in vivo*. We collected samples of rabbit carotid arteries 20 mins after intravenous injection of a mixture of the NO-producing protocells and hydroxyurea, and determined the blood vessel circumference from sectioned tissue. The stained sections revealed a statistically significant ($p < 0.05$) increase in the vessel circumference from 8.2 ± 1.1 mm in the control group (GOx-free protocells) to 9.7 ± 1.1 mm for injections of the GOx-containing protocells (Supplementary Fig. 21). This corresponded to an expanded vessel diameter of 3.1 mm, which was *ca.* 1.2 times larger than in the unrelaxed artery. In addition, the mean heart rate of the rabbit decreased from 222.0 ± 23.0 to 205.5 ± 19.0 min^{-1}, and the systolic blood pressure decreased from 144.0 ± 15.5 to 98.5 ± 18.0 mm Hg after administration of the GOx-containing protocells (Supplementary Fig. 22).

The above results suggested that under appropriate concentrations of endogenous glucose and supplemented hydroxyurea, the enzymatic activity of the injected protocells was sufficient to produce levels of NO production *in vivo* that were capable of triggering biochemical pathways of blood vessel vasodilation. However, given the reliance on micrograms of explanted blood vessels and possibility of artefacts associated with processing the thin sections, more detailed *in vivo* investigations will be required to substantiate the current findings.

Conclusions

In this paper, we demonstrate a novel protocell model based on the facile assimilation of erythrocyte membrane fragments and coacervate micro-droplets to produce membrane-bounded molecularly crowded cell-like objects that exhibit high hemocompatibility and improved blood circulation times. The presence of Hb and GOx within the membrane fragments and coacervate matrix, respectively, is exploited for the generation of a NO flux via a spatially coupled enzyme cascade in association with the transmission of an endogenous H_2O_2 signal. As a consequence, the protocells can be used to generate NO both *in vitro* within extracted aortic rings and *in vivo* via circulation within blood vessels. The concomitant vasoactivity leads to dilation of the pre-contracted aortic rings and provisional *in vivo* evidence for blood vessel vasodilation as a specific outcome of protocell functionality. We note that the direct release of NO doses to biological targets has some clinical limitations due to both the relative short lifetime

and high reactivity [61]; in this regard, surface modification of the hybrid protocells with specific cellular targets or immobilization of the coacervate vesicles in implanted medical devices might facilitate the safe transport of the cell-like vasoactive agents and their delivery to specific disease sites for required diagnostic applications.

Although our work is at an early stage and demonstrates a proof-of-concept, it should be relatively straightforward to advance the underpinning methodology to produce more complex biomembrane-enclosed coacervate vesicles that encompass increased levels of recognition and communication with living cells, including the exchange of genetic information. [15,42] In the longer term, our approach offers a novel pathway to the development of endogenously organized biocompatible cell-like objects and provides a step towards the fabrication of soft micro-bots for future applications in biomedicine, cellular diagnostics and bioengineering. The capability to encapsulate a variety of therapeutic payloads also provides new prospects for the development of coacervate-based protocells as novel theragnostic biocarriers for the simultaneous treatment and monitoring of diseases with enhanced therapeutic efficiency. In this respect, it seems probable that the polyelectrolyte (DEAE-dextran) and sheep erythrocyte membrane fragments associated with the protocells will be immunogenic as currently configured. Thus, the design and application of vasoactive coacervate vesicles comprising endogenous macromolecules will be the focus of future studies on *in vivo* activity.

Methods

Preparation of erythrocyte membrane fragments. Erythrocyte membrane fragments were derived from sheep red blood cells by hypotonic treatment. 40 mL of an aqueous suspension of erythrocytes (40% v/v) were centrifuged at 2000 rpm for 10 min at 4 °C. The resulting pellet was washed with DPBS and then repeated three times. Hemolysis was undertaken by addition of a 0.25-diluted DPBS solution followed by incubating the erythrocytes in an ice bath for at least 1 h. The lysed cells were centrifuged at 4,000 rpm for 20 min and the sediment containing the erythrocyte membranes was collected and washed with DPBS twice and then freeze-dried. Samples were subsequently re-dispersed by sonication in water at pH 7 at a concentration of 0.25 mg·mL^{-1}.

Preparation of erythrocyte membrane-encapsulated GOx-containing coacervate vesicles. Aqueous suspensions of coacervate micro-droplets with positive surface potential (+15.1 ± 1.7 mV) were prepared by mixing aqueous solutions of DEAE-dextran (1 mL, 10 mg·mL^{-1}, pH = 7.5) and *ds*DNA (0.5 mL, 10 mg·mL^{-1}, pH = 7.5) at a DEAE-dextran : DNA w/w ratio of 2 : 1). GOx was sequestered into the coacervate droplets by adding the enzyme to the DEAE-dextran solution prior to addition of *ds*DNA. To prepare the erythrocyte membrane-encapsulated coacervate protocells, 1 mL of the above coacervate suspension was added dropwise to a dispersion of sonicated erythrocyte membrane fragments (2 mL, 0.25 mg·mL^{-1}), and the mixture shaken gently and then incubated for 10 min at room temperature. The membrane-enclosed protocells were allowed to sediment and any residual erythrocyte fragments in the supernatant were then removed.

Hemolysis assays. Hemolytic activity of coacervate droplets was measured using a colorimetric method. Briefly, sheep erythrocyte cells in DPBS (100 µL, 40% v/v) were incubated with a suspension of erythrocyte membrane-coated DEAE-dextran/DNA coacervate micro-droplets (300 µL, 0.04-2.25 mg·mL^{-1}, isotonic DPBS) or a dispersion of uncoated DEAE-dextran/DNA micro-droplets (300 µL, 0.04-2.25 mg·mL^{-1}, isotonic DPBS) for 90 min at 37 °C. Alternatively, the DPBS erythrocyte cell suspension (100 µL, 40% v/v) was added to ultrapure water (300 µL) and left for 90 min at 37 °C. In each case, the samples were then centrifugated at 2,000 rpm for 20 min, and hemolysis was monitored spectroscopically by measuring the absorption at 540 nm of the hemolytic components released to the supernatant.

Blood circulation and *in vivo* tissue distribution. Blood circulation profiles were determined using erythrocyte membrane-enclosed coacervate vesicles or uncoated coacervate droplets (control) loaded with a Cy5 fluorescent dye in the coacervate matrix. Experiments were performed on New Zealand white rabbits (n = 6 ~~independent rabbits~~ per group~~, 2.5–3.0 kg~~). A suspension of the Cy5-loaded coacervate vesicles (2 mL kg^{-1}, containing 3.5 mg mL^{-1} coacervate microdroplets, 10 µg mL^{-1} Cy5) was injected. ~~through the marginal ear vein~~. The same dose of Cy5-loaded membrane-free coacervate droplets was also tested in parallel as a control. 500 µL of blood were collected at different time intervals after injection. The collected blood samples were collected in a 96-well plate for fluorescence measurements. The half-life values for blood circulation were obtained by first-order exponential decay fitting.

In vivo tissue biodistribution experiments were performed on New Zealand white rabbits (n = 6 ~~independent rabbits~~ per group~~, 2.5–3.0 kg~~). A suspension of erythrocyte membrane-enclosed Cy5-loaded

coacervate protocells (2 mL kg^{-1}, containing 3.5 mg mL^{-1} coacervate microdroplets, 10 μg mL^{-1} Cy5) was injected. ~~through the marginal ear vein~~. 6 rabbits were randomly selected and euthanized 2 and 24 h after injection. The collected organs (liver, kidney, spleen, lung, heart) and blood were collected, carefully washed, weighed and then homogenized in 1 mL PBS. The fluorescence intensity of each sample was determined using an Infinite M1000 multiplate reader. *In vitro* fluorescence imaging of tissues and blood were collected on a IVIS Lumina Ⅱ imaging system. Total weight of blood was estimated as 7% of rabbit body weight.

Protocell-mediated generation of NO. The enzyme cascade-mediated generation of NO by erythrocyte membrane fragment-coated DEAE-dextran/DNA coacervate vesicles was conducted in DPBS buffer (pH =7.4) containing 3.5 mg mL^{-1} of the bio-derived protocells containing entrapped GOx (200 nM). The cascade reaction was initiated by adding different amounts of glucose (0-20 mM) and hydroxyurea (0-10 mM). Peroxidase-mediated NO generation was quantified using a Greiss reagent colorimetric assay. Detection of the GOx-generated H_2O_2 intermediate and Hb-generated NO product in the protocells was undertaken using fluorescence microscopy imaging in the presence of Amplex red and DAF-2 probes, respectively.

***In vitro* NO generation and vasodilation.** Isometric aortic tension measurements were conducted *in vitro* according to previous protocols[62,63]. ~~New Zealand white rabbits (Hunan Taiping Biological Technology) were anesthetized by injecting 10% chloral hydrate (1.2 mL·kg^{-1}) into their marginal ear vein.~~ After New Zealand white rabbits were anesthetized, the thoracic aorta was quickly removed, and the extracted aorta cut into rings (n = 6 aorta rings per group, 18 aorta rings, 6 rabbits). One end of each ring was tied to a fixed hook and the other to a force transducer. Experiments were conducted in individual vessel bath chambers containing 20 mL of Krebs-Henseleit solution (NaCl 118 mM, KCl 4.7 mM, $CaCl_2$ 2.4 mM, KH_2PO_4 1.2 mM, $MgSO_4$ 2.4 mM, $NaHCO_3$ 25 mM, glucose 11.1 mM, pH=7.4) under physiological O_2 conditions and maintained at 37°C. After equilibration for 5 min, 60 mM KCl solution was added using a syringe. When the strip attained equilibrium tension, 1 mL of a solution containing hydroxyurea and a suspension of erythrocyte membrane-coated GOx-loaded DEAE-dextran/*ds*DNA coacervate protocells was added to the glucose-containing mixture (final concentrations: 0.5 mg mL^{-1} coacervate vesicles; 20 nM GOx, 2 mM hydroxyurea). Protocell-mediated generation of NO and the corresponding changes in tension force of the aortic ring were synchronized using a free radical analyzer with a NO electrode sensor (World Precision Instruments) and chart recorder connected to a HW200S/HW210S constant muscle test system (Chengdu Taimeng). The change in tension force (Δ *Tension*), and relaxation (%) were calculated as follows: (Δ *Tension*) = $F_t - F_0$; relaxation (%) = $(F_t - F_0)/F_0 \times 100\%$, where F_0 and F_t represent the tension force measured for the aorta before and after treatment with the NO-generating protocells, respectively.

***In vivo* NO generation.** New Zealand white rabbits (n = 6 ~~independent rabbits~~ per group~~, 2.5–3.0 kg~~) were injected with a suspension of erythrocyte membrane-enclosed GOx-loaded coacervate protocells containing hydroxyurea (2 mL kg^{-1}, containing 3.5 mg mL^{-1} coacervate microdroplets, 200 nM GOx, 20 mM hydroxyurea). Glucose was not added. Three groups (GOx-containing coacervate protocells without hydroxyurea; hydroxyurea alone; GOx-free coacervate protocells) were used as control. Blood was

collected at different time intervals after injection and NO concentrations were determined using a NO electrode sensor (World Precision Instruments).

Rabbits were euthanized and the carotid arteries collected. The arteries were incubated for 30 min in the dark with DAF-FM DA (10 μM, 3-amino, 4-aminomethyl-2',7'-difluorescein, diacetate), a NO-specific intracellular fluorescent probe. Then the carotid arteries were washed and separated into two sections randomly. One section was used to obtain fluorescence images on a IVIS Lumina Ⅱ imaging system and the other section was stored in liquid nitrogen for cryostat sectioning. For cryostat sectioning, the extracted artery rings were fixed in OCT embedding compound and frozen at -20 ℃. Sections (8 μm) were cut with a CM1850 cryostat (Leica Inc., Deerfield, IL, USA), and then mounted on slides and cover slips. Hoechst dye was used to stain the cell nucleus for observation. The samples were imaged by LSCM with a 10× objective.

***In vivo* blood vessel vasodilation.** New Zealand white rabbits (n=6 ~~independent rabbits~~ per group~~, 2.5-3.0 kg~~) were anesthetized ~~with 10% chloral hydrate (1.2 mL·kg^{-1})~~ and injected with a suspension of erythrocyte membrane-coated GOx-loaded DEAE-dextran/*ds*DNA coacervate protocells containing hydroxyurea (2 mL kg^{-1}; containing 3.5 mg mL^{-1} protocells, 200 nM GOx, 20 mM hydroxyurea). Glucose was not added. The heart rate and blood pressure were monitored with 3M Littmann 3200BK Electronic Stethoscope and SunTech Vet20 sphygmomanometer, respectively. Subsequently, the rabbits were euthanized, and the carotid artery was collected 20 in after injection. The blood vessels were fixed in 10% neutral buffered formalin, embedded in paraffin wax, sectioned at 4 μm, and processed for routine histology with hematoxylin and eosin stain. Morphometric analysis was carried out using an inverted microscope (Nikon Eclipse Ts2R) with a 4× objective.

Statistical analyses. Statistical analyses were performed using Origin 6.5. Student's t-tests were used for comparison between two groups according to data distribution. Values were normally distributed, and the variance was similar between compared groups. $P < 0.05$ was considered statistically significant.

Animal experiments. A total of 72 New Zealand white rabbits of both sexes (2.5-3.0 kg) were used and allocated to multiple studies as described in Table S1. New Zealand white rabbits were anesthetized by injecting 10% chloral hydrate (1.2 mL·kg^{-1}) into their marginal ear vein. The suspensions of protocells were injected through the marginal ear vein. Procedures with the cell and animal experiments used in this study were performed in accordance with the Guide of Hunan University for the Care and Use of Laboratory Animals and were approved by the Committee on Animal Care of Hunan University (No. SYXK (Xiang) 2013-0001).

Data availability

The main data are available within the paper and its Supplementary Information. The raw and analysed datasets are available from the authors on reasonable request.

References

1 Mage, P.L., Csordas, A.T., Brown, T., Klinger, D., Eisenstein, M., Mitragotri, S., Hawker, C., Soh, H.T. Shape-based separation of synthetic microparticles. *Nat. Mater.* **18**, 82-89 (2019).

2 Brenner, J.S., Pan, D.C., Myerson, J.W., Marcos-Contreras, O.A., Villa, C.H., Patel, P., Hekierski, H., Chatterjee, S., Tao, J.Q., Parhiz, H., Bhamidipati, K., Uhler, T.G., Hood, E.D., Kiseleva, R.Y., Shuvaev, V.S., Shuvaeva, T., Khoshnejad, M., Johnston, I., Gregory, J.V., Lahann, J., Wang, T., Cantu, E., Armstead, W.M., Mitragotri, S., Muzykantov, V. Red blood cell-hitchhiking boosts delivery of nanocarriers to chosen organs by orders of magnitude. *Nat. Commun.* **9**, 2684 (2018).
3 Sercombe, L., Veerati, T., Moheimani, F., Wu, S.Y., Sood, A.K., & Hua, S. Advances and challenges of liposome assisted drug delivery. *Front Pharmacol.* **6**, 286 (2015).
4 Monteiro, N., Martins, A., Reis, R.L., & Neves, N.M. Liposomes in tissue engineering and regenerative medicine. J. R. Soc. Interface. 11, 20140459 (2014).
5 Zylberberg, C., Gaskill, K., Pasley, S., & Matsevic. S. Engineering liposomal nanoparticles for targeted gene therapy. *Gene Ther.* **24**, 441–452 (2017).
6 Petersen, A.L., Hansen, A.E., Gabizon, A., & Andresen, T.L. Liposome imaging agents in personalized medicine. *Adv. Drug Deliv. Rev.* **64**, 1417-1435 (2012).
7 Rikken, R. S. M., Engelkamp, H., Nolte, R. J. M., Maan, J. C., van Hest, J. C. M., Wilson, D. A., & Christianen, P. C. M. Shaping polymersomes into predictable morphologies via out-of-equilibrium self-assembly. *Nat. Commun.* **7**, 12606 (2016).
8 Che, H., Cao S., & van Hest, J. C. M. Feedback-induced temporal control of "breathing" polymersomes to create self-adaptive nanoreactors. *J. Am. Chem. Soc.* **140**, 5356–5359 (2018).
9 Li, M., Harbron, R., Weaver, J., Binks, B., & Mann, S. Electrostatically gated membrane permeability in inorganic protocells. *Nat. Chem.* **5**, 529–536 (2013).
10 Huang, X., Li, M., Green, D. C., Williams, D. S., Patil, A. J., & Mann, S. Interfacial assembly of protein–polymer nano-conjugates into stimulus-responsive biomimetic protocells. *Nat. Commun.* **4**, 2239 (2013).
11 Huang, X., Patil, A. J., Li, M. & Mann, S. Design and construction of higher-order structure and function in proteinosome-based protocells. *J. Am. Chem. Soc.* **136**, 9225–9234 (2014).
12 Kumar, P. B. V. V. S., Patil, A. J. & Mann, S. Enzyme-powered motility in buoyant organoclay/DNA protocells. *Nat. Chem.* **10**, 1154 (2018).
13 Jang, W.-S., Kim, H. J., Gao, C., Lee, D. H., & Hammer, D. A. Enzymatically powered surface-associated self-motile protocells. *Small* **14**, 1801715 (2018).
14 Rodríguez-arco, L., Li, M., & Mann, S. Phagocytosis-inspired behaviour in synthetic protocell communities of compartmentalized colloidal objects. *Nat. Mater.* **16**, 857–863 (2017).
15 Qiao, Y., Li, M., Booth, R., & Mann, S. Predatory behaviour in synthetic protocell communities. *Nat. Chem.* **9**, 110-119 (2017).
16 Joesaar, A., Yang, S., Bögels, B., Linden, A.V.D., Pieters, P., Kumar, B. V. V. S. P., Dalchau, N., Phillips, A., Mann, S., & de Greef, T.F.A. DNA-based communication in populations of synthetic protocells. *Nat. Nanotechnol.* **14**, 369–378 (2019).
17 Sun, S., Li, M., Dong, F., Wang, S., Tian, L., & Mann, S. Functional activation and chemical signaling in clay-based colloidosomes. *Small* **12**, 1920 (2016).
18 Schwarz-Schilling, M., Aufinger, L., Muckl, A., & Simmel, F. C. Chemical communication between bacteria and cell-free gene expression systems within linear chains of emulsion droplets. *Integr. Biol.* **8**, 564 (2016).
19 Adamala, K.P., Martin-Alarcon, D.A., Guthrie-Honea, K. R., & Boyden, E. S. Engineering genetic circuit interactions within and between synthetic minimal cells. *Nat. Chem.* **9**, 431 (2017).
20 Tang, T-Y.D., Cecchi, D., Fracasso, G., Accardi, D., Coutable-Pennarun, A., Mansy, S. S., Perriman, A. W., Anderson, J. L. R., & Mann, S. Gene-mediated chemical communication in synthetic protocell communities. *ACS Synth. Bio*. **7**, 339 (2018).
21 Gobbo, P., Patil, A. J., Li, M., & Mann, S. Programmed assembly of synthetic protocells into contractile prototissues. *Nature Mater.* **17**, 1145-1153 (2018).
22 Koga, S., Williams, D. S., Perriman, A. W., & Mann, S. Peptide/nucleotide micro-droplets as a step towards a membrane-free protocell model. *Nat. Chem.* **3,** 720–4 (2011).
23 Merindol, R., Loescher, S., Samanta, A., & Walther, A. Pathway-controlled formation of mesostructured all-DNA colloids and superstructures. *Nat. Nanotechnol.* **13**, 730-738 (2018).
24 Martin, N., Douliez, J.-P., Qiao, Y., Booth, R., Li, M., & Mann, S. Antagonistic chemical coupling in self-reconfigurable host-guest protocells. *Nat. Commun.* **9**, 3652 (2018).

25 Tian, L., Li, M., Liu, J., Patil, A. J., Drinkwater, B. W., & Mann, S. Non-equilibrium spatiotemporal sensing within acoustically patterned two-dimensional protocell arrays. *ACS Cent. Sci.* **4**, 1551 (2018).
26 Drobot, B., Inglesias-Artola, J. M., Le Vay, K., Mayr, V., Kar, M., Kreysing, M., Mutschler, H. & Tang, T. Y. D. Compartmentalised RNA catalysis in membrane-free coacervate protocells. *Nat. Commun.* **9**, 3643 (2018).
27 Poudyal, R. R., Guth-Metzler, R. M., Veenis, A. J., Frankel, E. A., Keating, C. D., & Bevilacqua, P. C. Template-directed RNA polymerization and enhanced ribozyme catalysis inside membraneless compartments formed by coacervates. *Nat. Commun*. **10**, 490 (2019).
28 Zhang, Y., Baekgaard Laursen, M. & Städler, B. Small subcompartmentalised microreactors as support for hepatocytes. *Adv. Health. Mater.* **6**, 1601141 (2017).
29 Balasubramanian, V., Correia, A., Zhang, H., Fontana, F., Mäkilä, E., Salonen, J., Hirvonen, J., & Santos, H.A. Biomimetic engineering using cancer cell membranes for designing compartmentalised nanoreactors with organelle- like functions. *Adv. Mater.* **29**, 1605375 (2017).
30 Godoy Gallardo, M., Labay, C., Jansman, M. M. T., Ek, P. K. & Hosta-Rigau, L. Intracellular microreactors as artificial organelles to conduct multiple enzymatic reactions simultaneously. *Adv. Health. Mater.* **6**, 1601190 (2017).
31 Thingholm, B., Schattling, P., Zhang, Y. & Städler, B. Subcompartmentalised nanoreactors as artificial organelle with intracellular activity. *Small* **12**, 1806–1814 (2016).
32 Tanner, P., Balasubramanian, V. & Palivan, C. G. Aiding nature's organelles: artificial peroxisomes play their role. *Nano Lett.* **13**, 2875–2883 (2013).
33 C. Sieber, S., Goers, R., Najer, A., Spulber, M., Onaca-Fischer, O., Huwyler, J., & Palivan, C.G. Biomimetic artificial organelles with in vitro and in vivo activity triggered by reduction in microenvironment. *Nat Commun.* **9**, 1127 (2018).
34 P. M. Gardner, K. Winzer, & B.G. Davis, Sugar synthesis in a protocellular model leads to a cell signalling response in bacteria. *Nat. Chem.* **1**, 377-383 (2009).
35 Lentini, R., Santero, S. P., Chizzolini, F., Cecchi, D., Fontana, J., Marchioretto, M., Del Bianco, C., Terrell, J. L., Spencer, A. C., Martini, L., Forlin, M., Assfalg, M., Dalla Serra, M., Bentley, W. E., & Mansy, S. S. Integrating artificial with natural cells to translate chemical messages that direct E. coli behaviour. *Nat. Commun.* **5**, 4012 (2014).
36 Lentini, R., Yeh Martin, N., Forlin, M., Belmonte, L., Fontana, J., Martini, L., Cornella, M., Tamburini, S., Bentley, W.E., Jousson, O., & Mansy, S.S. Two-way chemical communication between artificial and natural cells. *ACS Cent. Sci.* **3**, 117–123 (2017).
37 Xia, Y., Wu, J., Wei, W., Du, Y., Wan, T., Ma, X., An, W., Guo, A., Miao, C., Yue, H., Li, S., Cao, X., Su, Z., & Ma, G. Exploiting the pliability and lateral mobility of Pickering emulsion for enhanced vaccination. *Nat Mater.* **17**, 187-194 (2018).
38 Zhou, Y., Song, J., Wang, L., Xue, X., Liu, X., Xie, H., & Huang, X. In situ gelation-induced death of cancer cells based on proteinosomes. *Biomacromolecules* **188**, 2446-2453 (2017).
39 Chen, Z., Wang, J., Sun, W., Archibong, E., Kahkoska, A.R., Zhang, X., Lu, Y., Ligler, F.S., Buse, J.B., & Gu, Z. Synthetic beta cells for fusion-mediated dynamic insulin secretion. *Nat. Chem. Bio.* **14**, 86–93 (2018).
40 Crosby, J., Treadwell, T., Hammerton, M., Vasilakis, K., Crump, M.P., Williams, D. S., & Mann, S. Stabilization and enhanced reactivity of actinorhodin polyketide synthase minimal complex in polymer/nucleotide coacervate droplets. *Chem. Commun.* **48**, 11832-11834 (2012).
41 Sokolova, E., Spruijt, E., Hansen, M.M., Dubuc, E., Groen, J., Chokkalingam, V., Piruska, A., Heus, H.A., & Huck, W.T. Enhanced transcription rates in membrane-free protocells formed by coacervation of cell lysate. *Proc. Natl. Acad. Sci. U.S.A.* **110**, 11692-11697 (2013).
42 Tang, T.Y.D., van Swaay, D., deMello, A., Anderson, J. L. R., & Mann, S. In vitro gene expression within membrane-free coacervate protocells. *Chem. Commun.* **51**, 11429-11432 (2015).
43 T.-Y. D. Tang, C. Rohaida Che Hak, A. J. Thompson, M. K. Kuimova, D. S. Williams, A. W. Perriman & S. Mann, Fatty acid membrane assembly on coacervate microdroplets as a step towards a hybrid protocell model. *Nat. Chem.* **6**, 527–533 (2014).
44 Mason, A. F., Buddingh, B. C., Williams, D. S., & Van Hest, J. C. M. Hierarchical self-assembly of a copolymer-stabilized coacervate protocell. *J. Am. Chem. Soc.* **139**, 17309–17312 (2017).
45 Fothergill, J., Li, M., Davis, S. A., Cunningham, J. A. & Mann, S. Nanoparticle-based membrane assembly and silicification in coacervate micro-droplets as a route to complex colloidosomes. *Langmuir* **30**, 14591–14596 (2014).

46 Deng, N. N., & Huck, W. T. S. Microfluidic formation of monodisperse coacervate organelles in liposomes. *Angew. Chem. Int. Ed.* **56**, 9736–9740 (2017).
47 Long, M. S., Cans A. S., & Keating, C. D. Budding and asymmetric protein microcompartmentation in giant vesicles containing two aqueous phases. *J. Am. Chem. Soc.* **130**, 756–762 (2008).
48 Booth, R., Qiao, Y., Li, M., & Mann, S. Spatial positioning and chemical coupling in coacervate-in-proteinosome protocells. *Angew. Chem. Int. Ed.* https://doi.org/10.1002/anie.201903756 (2019).
49 Blocher, W. C., & Perry, S. L. Complex coacervate-based materials for biomedicine. *WIREs Nanomed. Nanobiotechnol.* **9**, e1442 (2017).
50 Chu, H., Gao, J., Chen, C.W., Huard, J., & Wang, Y. Injectable fibroblast growth factor-2 coacervate for persistent angiogenesis. *Proc. Natl. Acad. Sci. U. S. A.* **108**, 13444-13449 (2011).
51 Chen, W.C., Lee, B.G., Park, D.W., Kim, K., Chu, H., Kim, K., Huard, J., & Wang, Y. Controlled dual delivery of fibroblast growth factor-2 and Interleukin-10 by heparin-based coacervate synergistically enhances ischemic heart repair. *Biomaterials.* **72**, 138-151 (2015).
52 Chu, H., Chen, C.W., Huard, J., & Wang, Y. The effect of a heparin-based coacervate of fibroblast growth factor-2 on scarring in the infarcted myocardium. *Biomaterials*. **34**, 1747-1756 (2013).
53 Hu, C.M., Zhang, L., Aryal, S., Cheung, C., Fang, R.H., & Zhang, L. Erythrocyte membrane-camouflaged polymeric nanoparticles as a biomimetic delivery platform. *Proc. Natl. Acad. Sci. U. S. A.* **108**, 10980-10985 (2011).
54 Hu, C.M., Fang, R.H., Luk, B.T., & Zhang, L. Nanoparticle-detained toxins for safe and effective vaccination. *Nat Nanotechnol.* **8**, 933-938 (2013).
55 Sokol, R. J., Heubi, J. E., Iannaccone, S., Bove, K. E., & Balistreri, W. F. Mechanism causing vitamin e deficiency during chronic childhood cholestasis. *Gastroenterology* **85**, 1172-1182 (1983).
56 Huang, J. , Sommers, E. M. , Kim-Shapiro, D. B., & King, S. B. Horseradish peroxidase catalyzed nitric oxide formation from hydroxyurea. *J. Am. Chem. Soc.* **124**, 3473-3480 (2002).
57 Gewaltig, M.T., & Kojda, G. Vasoprotection by nitric oxide: mechanisms and therapeutic potential. *Cardiovasc. Res.* **55**, 250-260 (2002).
58 Cohen, R.A., Weisbrod, R.M., Gericke, M., Yaghoubi, M., Bierl, C., & Bolotina, V.M. Mechanism of nitric oxide–induced vasodilatation: refilling of intracellular stores by sarcoplasmic reticulum Ca^{2+} ATPase and inhibition of store-operated Ca^{2+} influx. *Circ. Res.* **84**, 210-219 (1999).
59 Wang, C., Trudel, L.J., Wogan, G.N., Deen, W.M. Thresholds of nitric oxide-mediated toxicity in human lymphoblastoid cells. *Chem. Res. Toxicol.* **16**, 1004-1013 (2003).
60 Pacher, P., Beckman, J.S., & Liaudet, L. Nitric oxide and peroxynitrite in health and disease.*Physiol Rev.* **87**, 315-424 (2007).
61 Yang, T., Zelikin, A.N., Chandrawati, R. Progress and promise of nitric oxide‐releasing platforms. *Adv. Sci.* **5**, 1701043 (2018).
62 Micheli, S. F., Failli, P., Mazzetti, L., Bani, D., Ciuffi, M., & Zilletti. L. Mechanical stretch reveals different components of endothelial‐mediated vascular tone in rat aortic strips. *Br. J. Pharmacol*. **131**, 1355-1362 (2000).
63 Fleming, I., Bauersachs, J., Schäfer, A., Scholz, D., Aldershvile, J., & Busse, R. Isometric contraction induces the Ca^{2+}-independent activation of the endothelial nitric oxide synthase. *Proc. Natl. Acad. Sci. U.S.A.* **96**, 1123-1128 (1999).

Acknowledgments
We thank the National Natural Science Foundation of China (21735002, 21575037, 21778016, 21675046), keypoint research program of Hunan province (2017DK2011) for financial support. The work was partly supported by the BBSRC (BB/P017320/1), the ERC Advanced Grant Scheme (EC-2016-ADG 740235), and BrisSynBio, a BBSRC/EPSRC Synthetic Biology Research Centre (BB/L01386X/1). We thank Dr. Can Xu for fruitful discussions, and Rencai Animal Hospital in Changsha for rabbit experiments.

Author Contributions
S.L., K.W., J.L., and S.M. conceived the experiments, S. L., Y.Z., Z. Z. and L.X. performed the experiments, All the authors undertook the data analysis, and S.L., J.L., and S.M. wrote the manuscript.

Competing interests
The authors declare no competing interests.

Additional information
Supplementary information is available in the online version of the paper. Reprints and permissions information is available online at www….. Correspondence and requests for materials should be addressed to J. L., S.M.

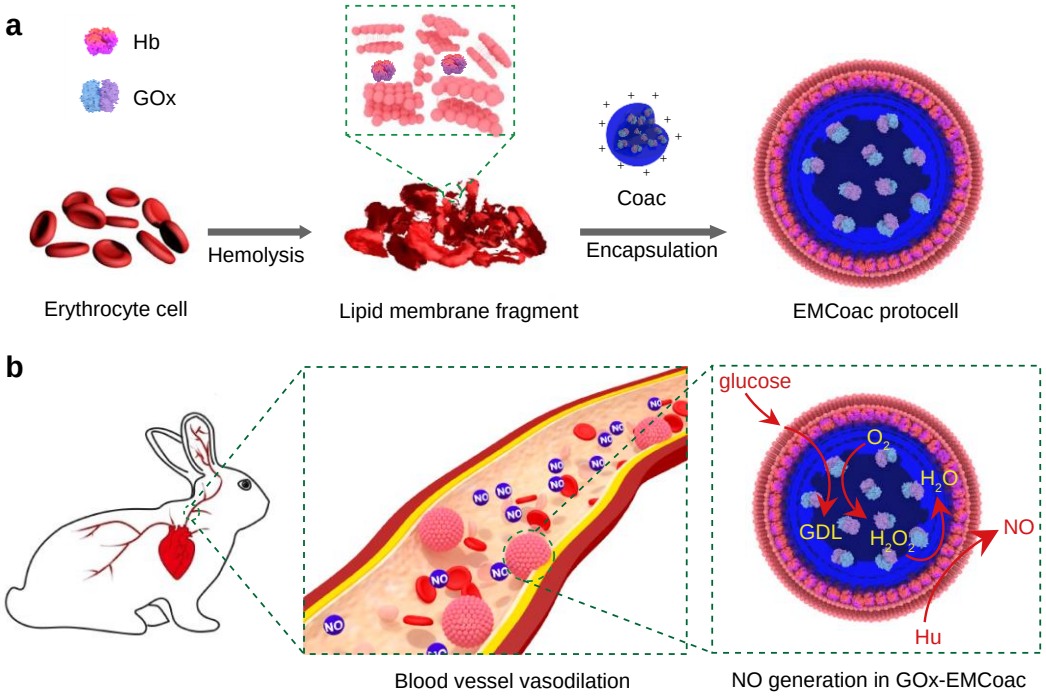

Figure 1. Structure and function of bio-derived hybrid protocells. (**a**) Scheme showing design and construction of enzymatically active erythrocyte membrane-encapsulated coacervate (EMCoac) protocells. Hemoglobin (Hb)-containing membrane fragments are extracted from fresh sheep blood *via* hypotonic hemolysis and then added to a suspension of positively charged DEAE-dextran/*ds*DNA coacervate micro-droplets containing glucose oxidase (GOx). Spontaneous assembly of the fragments at the droplet surface results in formation of biomembrane-coated molecularly crowded hybrid protocells. The bio-derived protocells exhibit enhanced hemocompatibility and display spatially confined peroxidase-like GOx/Hb cascade activity. (**b**) Illustration showing *in vitro* and *in vivo* GOx/Hb cascade generation of NO at micromolar concentrations in the presence of coacervate-sequestered enzyme substrates (glucose and hydroxyurea (Hu), respectively) as a step towards protocell-mediated blood vessel vasodilation. Hb and GOx are spatially positioned on the periphery and in the interior of the protocell bioreactor, respectively (GDL = gluconolactone).

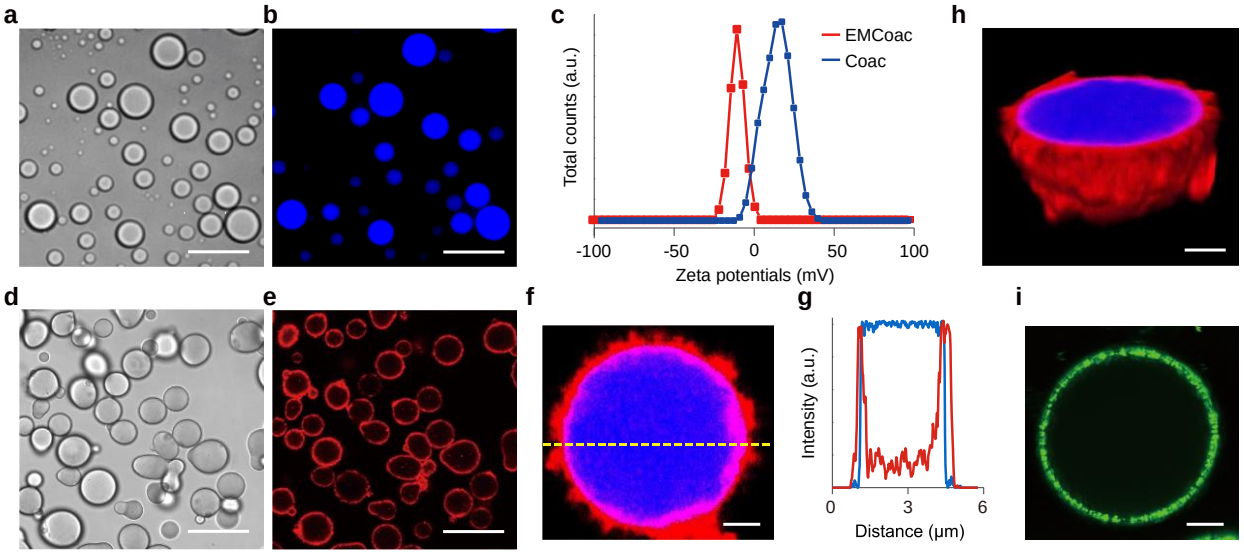

Figure 2. Construction and characterization of erythrocyte membrane-encapsulated coacervate protocells. (**a,b**) Optical bright field (**a**) and corresponding blue fluorescence (**b**) image of DNA binding Hoechst-33258-stained DEAE-dextran/*ds*DNA coacervate micro-droplets (DEAE-dextran : DNA = 2 : 1, w/w); scale bar, 10 μm. (**c**) Zeta potential profiles of an aqueous dispersion of DEAE-dextran/*ds*DNA coacervate micro-droplets at pH 7 before (Coac) and after (EMCoac) the addition of a suspension of Hb-containing erythrocyte membrane fragments showing charge reversal on formation of the biohybrid protocells. (**d,e**) Optical bright field (**d**) and corresponding red fluorescence (**e**) image of 1,1′-dioctadecyl-3,3,3′,3′-tetramethyl indocarbocyanine perchlorate (Dil)-stained membrane fragment-encapsulated coacervate micro-droplets showing the presence of a surrounding lipid-containing surface shell; scale bar, 10 μm. (**f-h**) Cross-sectional fluorescence microscopy image (**f**) and corresponding fluorescence intensity profile (**g**, dashed line in **f**), and associated 3D reconstructed image (**h**) of a single bio-derived hybrid protocell stained with Hoechst-33258 (blue fluorescence) and Dil (red fluorescence). The DNA-containing coacervate interior is uniform and continuous while the lipid shell derived from interfacial assembly of the erythrocyte membrane fragments is irregular; scale bars in **f** and **h**, 1 μm. (**i**) Fluorescence microscopy image of a single coacervate droplet showing preferential localization of FITC-Hb at the droplet surface. The sample was prepared by adding FITC-labelled Hb to the membrane extract prior to mixing with the coacervate droplets; scale bar, 1 μm.

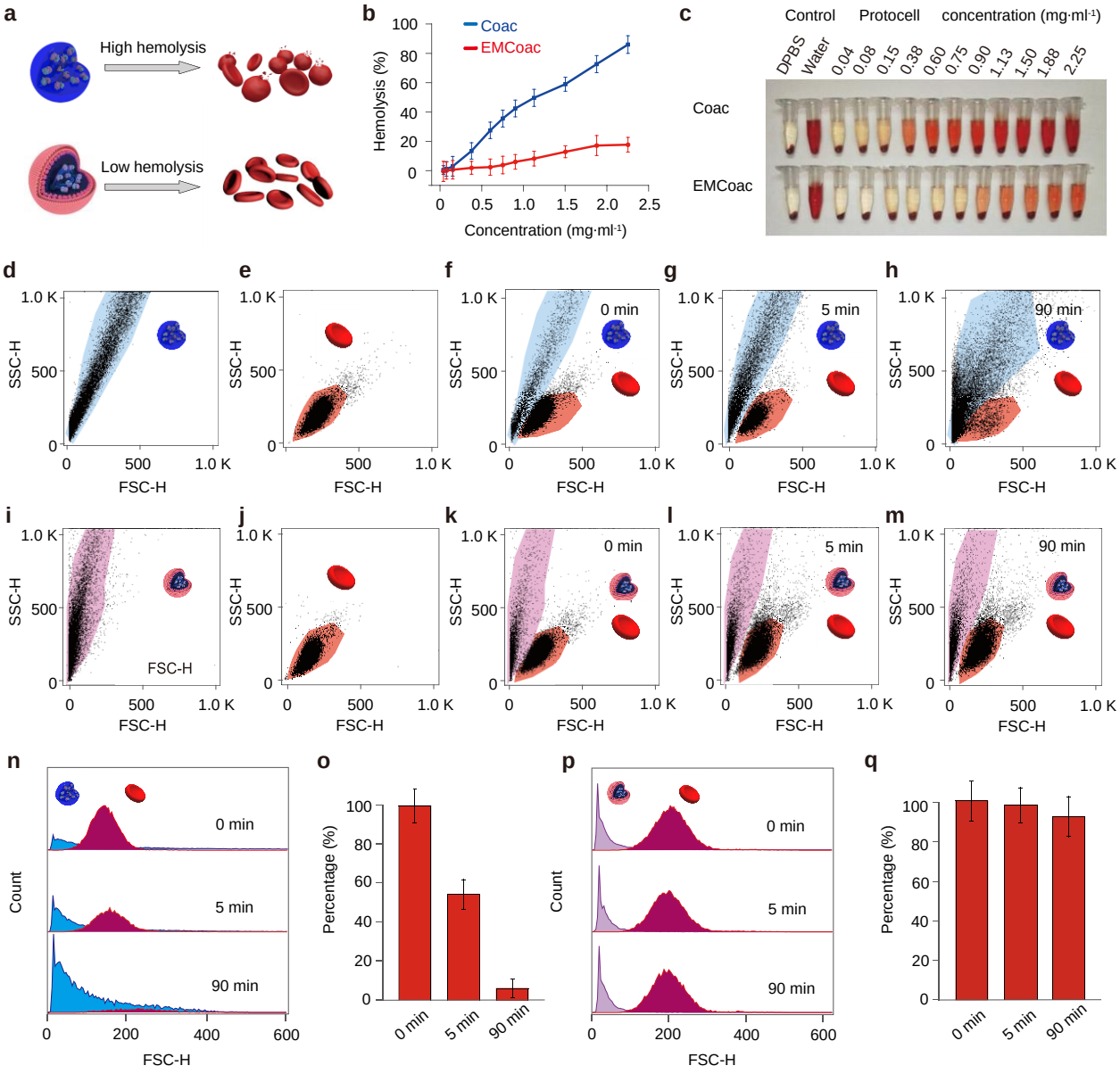

Figure 3. **Hemocompatibility of coacervate-based protocells.** (**a**) Illustration showing high hemolytic activity of membrane-free coacervate droplets (blue, top scheme) compared with low levels of red blood cell lysis in the presence of erythrocyte membrane-encapsulated coacervate protocells (red, bottom scheme). (**b**) Plot of percentage hemolysis against coacervate concentration for uncoated (Coac, blue) and erythrocyte membrane-coated (EMCoac, red) coacervate droplets. Data were determined from the spectroscopic analysis of supernatants obtained after centrifugation of samples 90 min after incubation of the erythrocytes with isotonic dispersions of the unmodified or modified coacervate droplets. (**c**) Photograph of the centrifuged samples used for the hemolysis assay shown in **b**; the intensity of the red coloration in the supernatant is indicative of the level of red blood cell lysis obtained in the presence of the coacervate-based protocells. (**d-h**) 2D dot plots of FSC-H *versus* SSC-H for single populations of membrane-less coacervate droplets (**d,** blue domain) or erythrocytes (**e**, red domain), and binary populations of uncoated coacervate droplets and erythrocytes recorded 0 (**f**), 5 (**g**) and 90 min (**h**) after mixing at room temperature showing progressive depletion of the red blood cell population and formation

of a new sub-population of erythrocyte membrane-coated coacervate droplets with relatively low FSC-H and high SSC-H values, respectively (see **h**). (**i-m**) 2D dot plots for single populations of erythrocyte membrane-encapsulated coacervate droplets (**i,** pink domain) or erythrocytes (**j**, red domain), and binary populations of membrane-coated coacervate droplets and erythrocytes recorded 0 (**k**), 5 (**l**) and 90 min (**m**) after mixing at room temperature showing minimal changes in the population number densities. Total number of particles counted, 20000; initial droplet: erythrocyte number ratio, 1 : 4). (**n,o**) Time-dependent FACS-derived FSC-H counts for binary populations of uncoated coacervate droplets (blue) and erythrocytes (red) (**n**), and corresponding histograms (**o**) showing coacervate-induced lysis of the red blood cells. (**p,q**) As for **n,o** respectively, but for mixtures of erythrocyte membrane-encapsulated coacervate droplets (pink) and erythrocytes (red) showing hemocompatibility of the enclosed protocells. Data in **b, o** and **q** represent mean values and first standard deviations (n = 3 per group). ~~determined from three experiments~~.

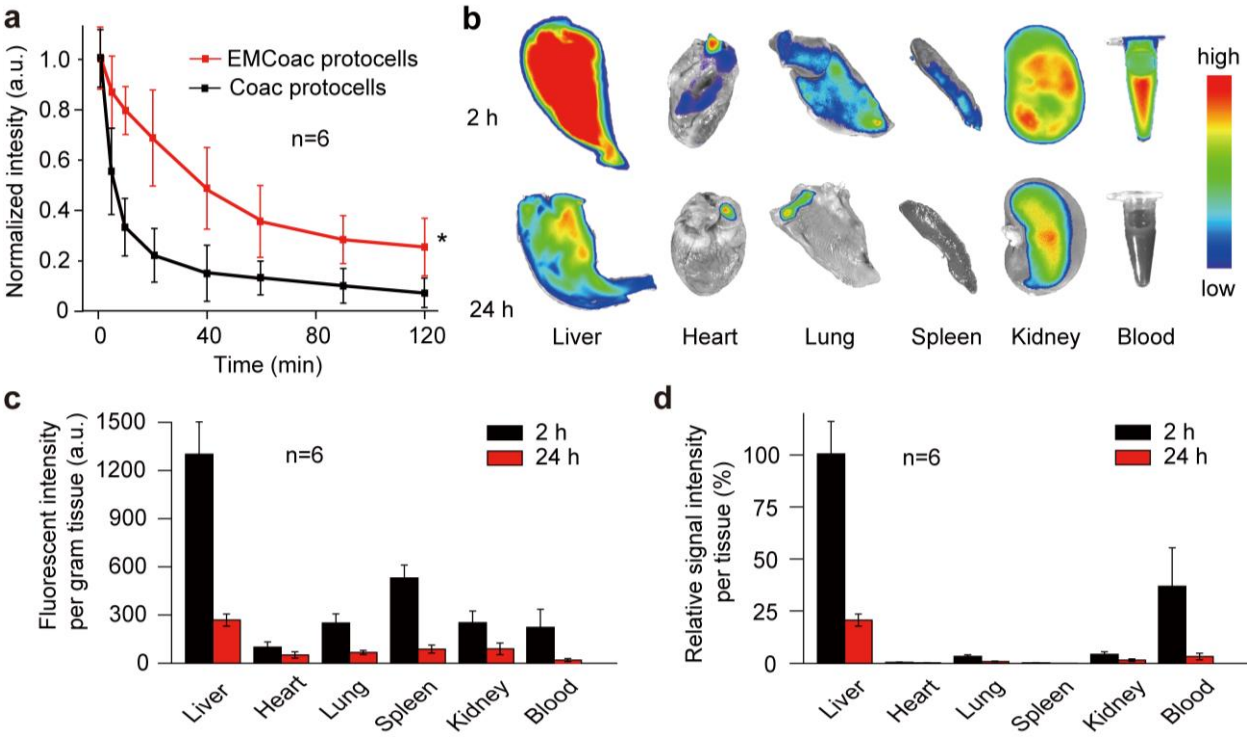

Figure 4. Blood circulation and *in vivo* biodistribution. (**a**) Blood clearance profiles of erythrocyte membrane-enclosed coacervate vesicles (EMCoac protocells, red) and membrane-free coacervate droplets (Coac protocells, black). Plots show changes in normalized fluorescence intensity for blood samples taken at various times after injection of the Cy5-loaded protocells (2 mL kg^{-1}, containing 3.5 mg mL^{-1} microdroplets, 10 µg mL^{-1} Cy5; rabbits (n = 6 per group) ; **P*= 0.035 compared to uncoated protocells). (**b**) *In vivo* distribution of erythrocyte membrane-enclosed coacervate vesicles in the major organs examined at 2 and 24 h after injection of the Cy5-loaded coacervate vesicles using an animal fluorescence imaging system. Injection conditions; 2 mL kg^{-1} containing 3.5 mg mL^{-1} microdroplets, 10 µg mL^{-1} Cy5; rabbits (n = 6 per group). Colour scale indicates level of fluorescence in the different tissues. (**c**) Plot showing fluorescence intensity per gram of tissue determined for samples shown in **b** after 2 and 24 h. (**d**) Corresponding plot showing relative signal intensity per tissue after 2 and 24 h. Fluorescence intensities were multiplied by the measured weight of the corresponding tissues. The blood weight was estimated as 7% of the total body weight.

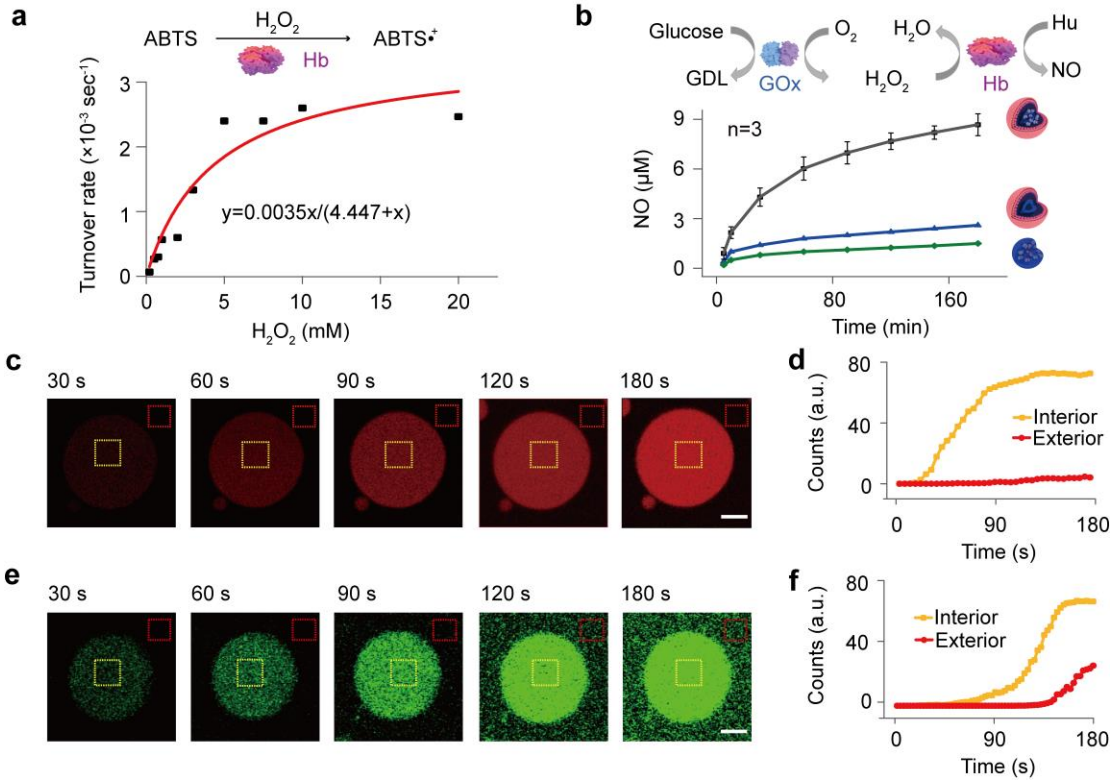

Figure 5. Protocell-mediated generation of NO. (**a**) Enzyme activity of an erythrocyte membrane extract showing turnover rate against hydrogen peroxide concentration for the Hb-mediated peroxidation of ABTS. The plot is fitted to Michaelis-Menten kinetics (K_m, 4.45 mM; K_{cat}, 7.05 s^{-1}) and indicates that the extracted Hb remains enzymatically active. (**b**) Reaction scheme and kinetic plots associated with a GOx/Hb enzyme cascade for the glucose-triggered production of NO. The process is spatially coupled between the Hb-containing membrane and GOx-containing interior of the erythrocyte membrane-coated coacervate vesicles (black plot) and operates via an internally generated H_2O_2 signal; vesicles, 3.5 mg·mL^{-1}; glucose, 5 mM; hydroxyurea (Hu), 2 mM; GDL, D-gluconolactone. Control plots for coacervate droplets without GOx (blue) or membrane extract (green) are also shown. Data represent mean values and first standard deviations (n=3 per group) ~~determined from three experiments~~. (**c-f**) Time-dependent fluorescence microscopy images of a single erythrocyte membrane-coated coacervate vesicle prepared as in (**b**) but in the presence of Amplex Red and DAF-2; images are recorded in the red (**c,d**) and green (**e,f**) fluorescence channels after addition of glucose (t = 0) and correspond to resorufin and NO production, respectively. Plots of fluorescence counts against time for delineated internal (dashed yellow boxes) and external regions (dashed red boxes) are shown in **d** and **f**. Scale bar, 2.0 μm.

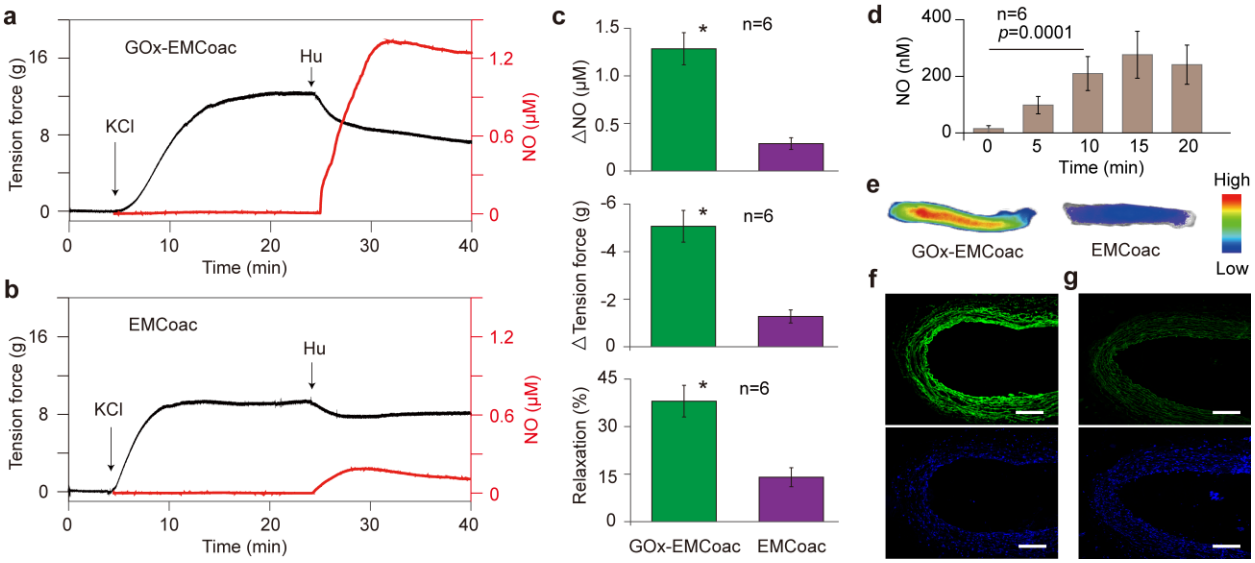

Figure 6. **Protocell-induced NO-mediated blood vessel vasodilation**. (**a,b**) Representative traces of *in vitro* aortic vasodilatation as determined by simultaneous measurement of the isometric tension force (black line) and NO concentration (red line) against time in the presence of erythrocyte membrane-coated coacervate protocells (0.5 mg mL^{-1}) with (**a**; GOx-EMCoac) or without (**b**; EMCoac) encapsulated GOx. The small quantity of NO (0.3 μM) and decrease in tension force (1.3 g; 14% relaxation) observed in the absence of GOx was attributed to the low-level degradation of hydroxyurea in blood media. (**c**) Bar charts of total increase in NO concentration (ΔNO), decrease in tension force (ΔTension force), and increase in vasodilatation (Relaxation %) obtained from experiments shown in **a** and **b.** **P* = 0.0001 compared to EMCoac protocells. (**d**) Plot showing time-dependent changes in blood NO concentrations in ~~New Zealand white~~ rabbits (~~2.5–3.0 kg,~~ n = 6 per group~~independent rabbits~~) after intravenous injection of hydroxyurea (20 mM) and GOx-loaded erythrocyte membrane-enclosed coacervate vesicles (2 mL kg^{-1}, containing 3.5 mg mL^{-1} coacervate microdroplets, 200 nM GOx). (**e**) Fluorescence images of bulk blood vessels stained with DAF-FM DA for detection of intracellular NO. The rabbits were administrated with GOx-containing coacervate protocells and hydroxyurea (GOx-EMCoac) or GOx-free coacervate protocells and hydroxyurea (EMCoac). (**f,g**) Fluorescence microscopy image of sectioned blood vessel tissue stained with DAF-FM DA (green fluorescence, NO production) and Hoechst-33258 (blue fluorescence, cell nuclei). The rabbits were administrated with GOx-containing coacervate protocells and hydroxyurea (**f**, GOx-EMCoac) or GOx-free coacervate protocells and hydroxyurea (**g**, EMCoac). Scale bars, 100 μm.